Comminution-induced Transient Frictional Behavior in Sheared Granular Halite

Chengrui Chang[1], Hiroyuki Noda[2], Yohei Hamada[3], Gonghui Wang[2], Chao Huang[4], and Tetsuo Yamaguchi[1]

[1]Department of Biomaterial Sciences, Graduate School of Agricultural and Life Sciences, The University of Tokyo, Tokyo, 1138657 Japan.

[2]Disaster Prevention Research Institute, Kyoto University, Uji, 6110011 Japan.

[3]Kochi Institute for Core Sample Research, Japan Agency for Marine-Earth Science and Technology (JAMSTEC), Nankoku, 7838502 Japan.

[4]Division of Earth and Planetary Sciences, Graduate School of Science, Kyoto University, Uji, 6110011 Japan.

Corresponding author: Tetsuo Yamaguchi (yamaguchi-tetsuo@g.ecc.u-tokyo.ac.jp)

Key Points:

- Sheared granular halite exhibits constant friction at small slip displacements and substantial weakening at large displacements.
- Characteristic slip lengths for constant friction and weakening decrease with normal stress and are characterized by similar exponents.
- The production, saturation, and overflow of fine particles in the shear zone are key factors determining transient frictional behavior.

Abstract

Drastic grain comminution is frequently observed in upper-crust faults and large rock avalanche deposits. Here we report our model experiments to elucidate the possible role of grain comminution in dry granular friction. We sheared halite (NaCl) grains with a ring-shear configuration at a constant slip rate under various normal stresses and investigated the post-slip structures of the experimental fault zones using micro X-ray computed tomography. Consequently, distinct frictional behaviors were observed: a constant friction regime at small slip displacements and a frictional weakening regime at large displacements. The characteristic slip lengths for the two regimes decreased with increasing normal stress and were characterized by approximately the same exponent, regardless of the initial grain size. We developed a theoretical model that considered the production, saturation, and overflow of fine particles in the shear zone and successfully reproduced the transient frictional behavior in the experiments.

Plain Language Summary

Grain comminution and structural evolution are common in natural settings, including earthquake faults and landslides. However, their role in granular friction remains poorly understood. We experimentally sheared breakable NaCl grains to simulate the processes in the growing fault zones and visualized their microstructures using micro- X-ray computed tomography (CT). Two distinct frictional behaviors were observed: a constant regime showing a high friction coefficient at small slip displacements, and a weakening regime with a substantial drop in friction at large slip displacements. The characteristic slip lengths for the two regimes decrease with increasing normal stress. Micro-observations revealed fine particles and extremely

localized shear planes. It was inferred that the frictional evolution was characterized by grain comminution mechanisms that continuously produce fine particles. Fine particles with low rolling friction serve as the interstitial granular fluid and accumulated in the porous medium once the shear started. The constant regime was dominated by sliding friction between large grains and terminated when the comminuted fine particles fully saturated the shear zone. Subsequently, the overflow of fine particles led to weakening by decreasing the effective normal stress between the large grains. We describe these processes using a simple theoretical model and reproduce the frictional behaviors.

1 Introduction

The constitutive properties and frictional behavior of faults are key factors in understanding diverse faulting processes. Many experimental studies have been conducted using various configurations such as double direct shear (e.g., Dieterich, 1972; 1978), rotary shear (e.g., Weeks and Tullis, 1985; Tsutsumi and Shimamoto, 1997), triaxial loading (e.g., von Kármán, 1911; Brace and Byerlee, 1966; Shimamoto et al., 1980), and large-scale biaxial friction (e.g., Dieterich, 1981; Yamashita et al., 2015; McLaskey and Yamashita, 2017). In these experimental studies, the shear zone thickness was in the order of several millimeters and could not increase owing to restricted slip displacement or gouge confinement. In contrast, the gouge thickness in natural faults is usually much greater than that in experimental faults (e.g., Engelder, 1974; Robertson 1982; Scholz, 1987; Chambon et al., 2006) and the energy dissipation and rupture processes within a thick layer differ from those at a distinct interface (Sibson, 2003). Furthermore, while most experimental configurations include gouges sandwiched between

consolidated host rocks, few studies have investigated the effects of unconsolidated and highly porous rocks and sediments, which are frequently involved in upper crust fault (e.g., Chester and Logan, 1986; Faulkner et al., 2010) and subduction zones (e.g., Polet and Kanamori, 2000; Kitajima and Saffer, 2014).

The cataclastic process is active in faulting processes and stimulates intense fracturing and crushing of grains (e.g., Borg et al., 1960; Griggs and Handin, 1960; Engelder, 1974; Kimura et al., 2007; Fossen, 2010). Apart from earthquake faults, large rock avalanches are another significant geophysical phenomenon that often exhibit thick deposits accompanied by extreme grain size reduction (e.g., Heim, 1932; Davies et al., 1999; Davies and McSaveney, 2002, 2009; Crosta et al., 2007) and results in large runouts (e.g., Heim, 1932; Hsü, 1975; Davies, 1982; Davies et al., 1999; Legros, 2002). Although their geometries, boundary conditions, and stress levels differ significantly from those of earthquake faults, shearing of dense granular flow is common (e.g., Siman-Tov and Brodsky, 2018), and the fine particles produced are considered to play an important role in the friction of the fault zone.

In this study, we aim to elucidate the mechanisms of grain comminution and structural evolution in a growing fault zone that developed in an unconsolidated and porous granular medium. Friction experiments were performed using a ring shear apparatus (Sassa et al., 2004) and a large volume of breakable grains. Halite (NaCl) has been frequently used as an analog for fault gouges because it reveals a wide variety of deformation mechanisms (e.g., Shimamoto, 1986; Hiraga and Shimamoto, 1987; Bos and Spiers, 2002; Kim et al., 2010; Noda and Shimamoto, 2010, 2012; Buijze et al., 2017) and is suitable for experimentally studying the frictional properties of grain comminution in faults. Notably, large and thick experimental fault zone was observed within the granular medium, as discussed in this paper. We then followed the

key mechanisms of grain comminution by combining frictional measurements, post-slip structural observations, and data analyses. Finally, we propose a theoretical model for the saturation and overflow of comminuted fine particles to interpret and reproduce our observations.

2 Materials and Methods

Angular-shaped granular halite (NaCl) with two different initial sizes, namely coarse-grained halite (~2-5 mm) and fine-grained halite (~0.425-0.85 mm), were used as model granular materials.

The experimental setup is schematically shown in Figure 1a. The ring-shear apparatus has previously been used in the studies of landslide behavior (e.g., Sassa and Lee, 1993; Sassa et al., 1996; 2004). Detailed specifications are outlined by Sassa et al. (2004). In each test, approximately 1.5 kg of granular halite were evenly distributed in a ring-shear box (outer and inner diameters of 18 and 12 cm, respectively, with a 10.9 cm maximum sample height). The upper shear box was stationary, while the lower shear box was spinning. The rubber edges were glued to the lower shear box separation to prevent grain leakage. The halite samples were sheared at a constant slip rate of 0.05 cm/s under three levels of normal stress: 0.2, 0.6, and 1.0 MPa. All experiments were completed in room-dry conditions (humidity ~50%) at 24°C. We applied 2 m slip displacement (Table S1 in the Supporting Information) unless otherwise noted. After each test, we carefully took out blocks from the shear zone. The shear-zone samples were cohesive and hard, as shown in Figures 1b and 1c. Post-experiment structural analyses of the halite fault zone were performed for three baseline runs in coarse-grained media using high-

resolution micro X-ray CT (Versa XRM-500 X-ray microscope). More details are provided in the "Expanded Methods" section and Table S1 in the Supporting Information.

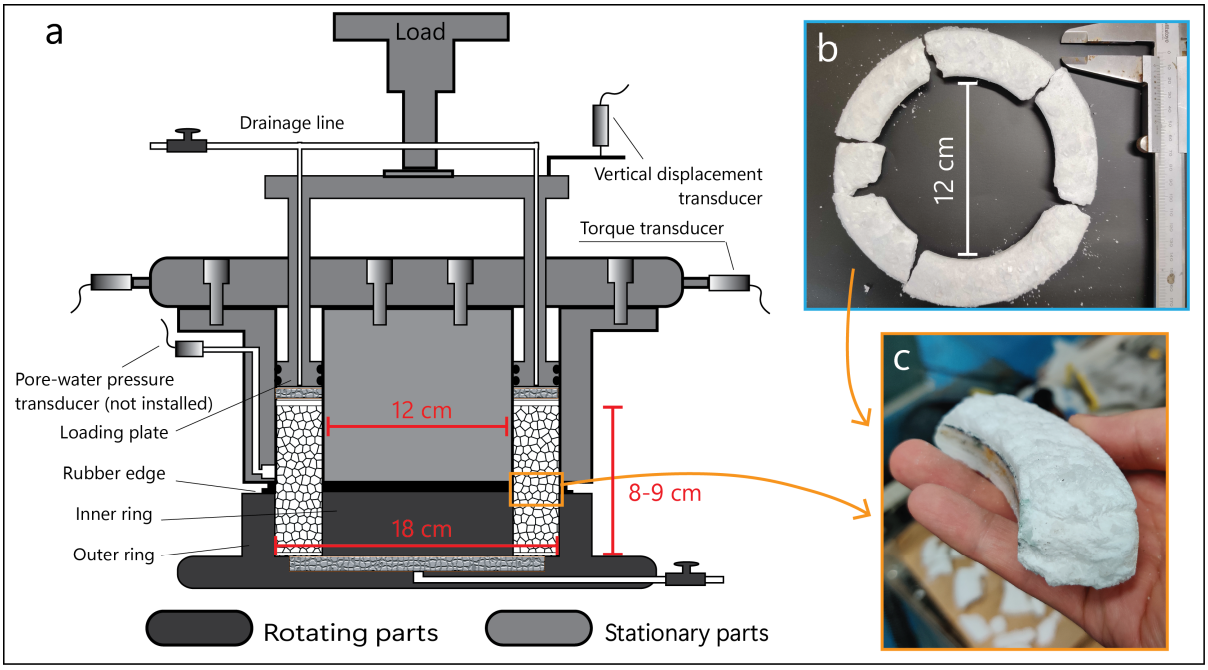

Figure 1. Ring-shear configuration and shear zones after testing. (a) Schematic of Ring-shear apparatus. (b) Top view of shear zone blocks for coarse-grained medium. (c) A shear zone block of coarse-grained medium.

3 Results

3.1 Frictional behavior

Figure 2 shows representative frictional behavior and micro X-ray CT observations. We used the moving average to smooth the data and emphasize the transient frictional behavior, as shown in Figures 2a (coarse-grained medium) and 2b (fine-grained medium). A comparison of raw and processed data is provided in the Supporting Information (Figure S1). Here, we present the evolution of the friction coefficient (μ) and sample height change (Δh) against the slip

displacement (δ). As shown in Figure 2a, all samples showed an increase in friction in the initial loading stage. For the experimental run performed under the lowest normal stress ($\sigma = 0.2$ MPa), the friction coefficient reached its peak and then remained at $\mu \approx 0.7$ until the test ended. The sample exhibited dilation and switched to continuous compaction after reaching the peak friction. In contrast, under intermediate normal stress ($\sigma = 0.6$ MPa), the friction started to weaken at a slip displacement of approximately 660 mm. Finally, substantial weakening was observed at a steady-state value $\mu \approx 0.43$. In addition, the height change indicated compaction during the initial phase. Under maximum normal stress ($\sigma = 1.0$ MPa), the friction remained relatively stable for a small displacement of ~ 200 mm. Rapid weakening was then initiated, and friction evolved to a significantly lower value of $\mu \approx 0.36$. The results of the fine-grained media are also shown in Figure 2b and are comparable to those of the coarse-grained media. The total change in height in the fine-grained medium was smaller than that in the coarse-grained medium.

Notably, substantial weakening occurred at small displacements when the normal stress was high, indicating that the evolution of friction was dependent on the normal stress. To observe frictional weakening under the lowest normal stress (0.2 MPa), we conducted friction experiments at large slip displacements (Figure S2 in Supporting Information). Consequently, weakening occurred after a significantly large slip displacement of ~7 m in the coarse-grained medium and ~5 m in the fine-grained medium.

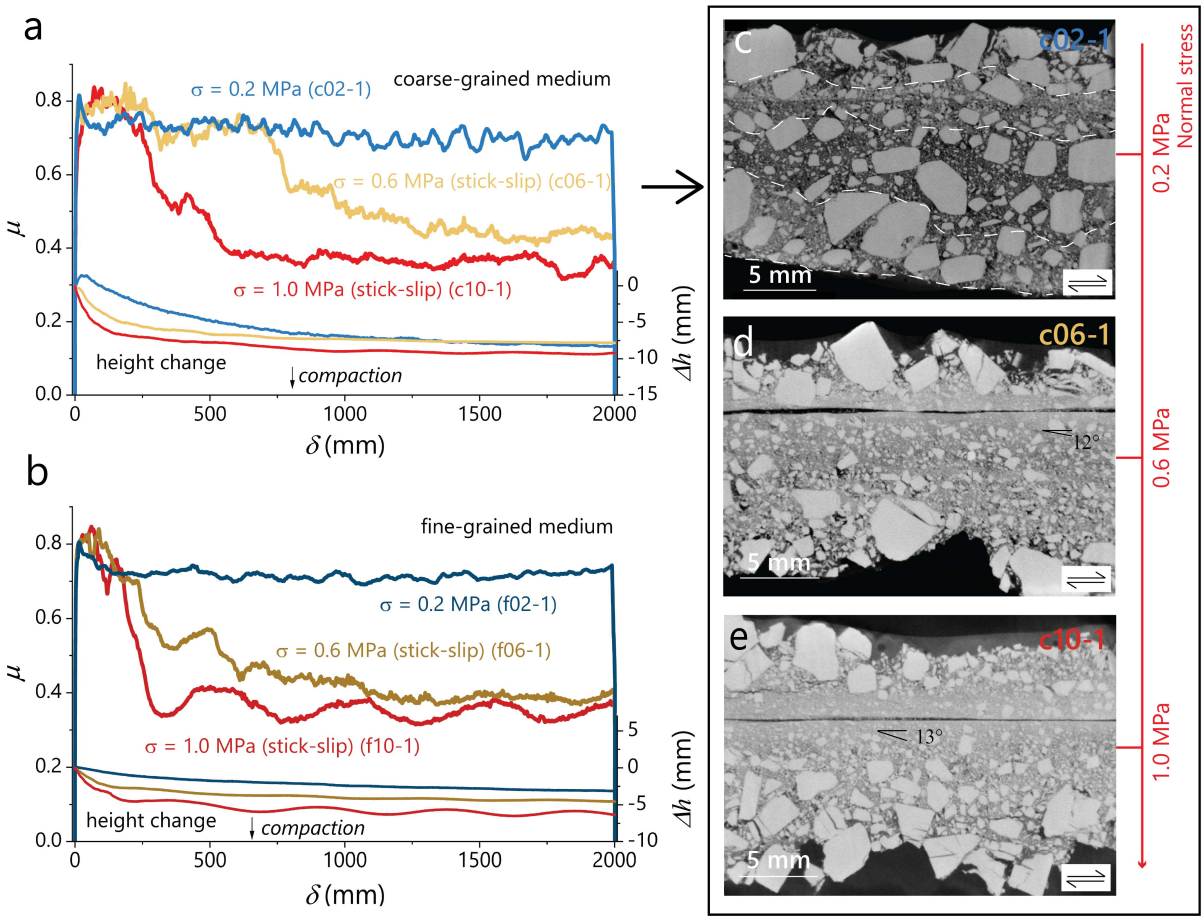

Figure 2. Representative frictional behaviors and micro-CT images. Frictional behaviors in coarse-grained (a) and fine-grained (b) media. Friction coefficient and height change plotted against slip displacement under different normal stresses. Cross sections of shear zone from experimental run after 2 m slip displacement, under (c) 0.2 MPa, (d) 0.6 MPa, and (e) 1.0 MPa.

3.2 Microstructures

Micro X-ray cross-sectional images (parallel to the shear direction) after 2 m slip displacement in the coarse-grained medium are shown in Figures 2c, 2d, and 2e. Drastic comminution processes were also observed. Many fine particles accumulated within a broad

domain, and their size was smaller than tens of microns, which is beyond the scanning resolution.

For the samples under 0.2 MPa, bright areas with a high density (circled with dashed lines) were observed, and the shear zone suggested characteristics of cataclasis between the bright and dense areas, as shown in Figure 2c. Although some voids were observed between the large grains, the large grains were loosely surrounded by comminuted fine particles.

The structures of the samples under large normal stress were significantly different, in which the progressive production of fine particles and well-developed shear planes were observed (Figures 2d and 2e). The shear planes were considerably flat with mild waviness. An evident shear texture was observed, with grain alignments of approximately 12-13°. A small number of fine particles remained in the gap between the slip surfaces, suggesting the local detachment of the upper and lower surfaces during motion. Generally, grains near the shear planes were intensively comminuted and densely compacted, whereas some large grains remained intact along the sliding surface.

4 Discussion

4.1 Data analysis

Two distinct frictional behaviors were identified in our experimental observations. A similar observation consisting of two regimes for crushable materials was reported by Hu et al. (2022). In Figure 3a, we describe our simple model, which comprises an initial constant regime and a weakening regime against slip displacement. Frictional evolution $\mu(\delta)$ is given by the following equation:

$$\mu(\delta) = \begin{cases} \mu_0 , & \delta < L_0 \\ (\mu_0 - \mu_{ss}) \exp\left(-\dfrac{\delta - L_0}{L_w}\right) + \mu_{ss} , & \delta \geq L_0 \end{cases} \quad (1)$$

where μ_0 and μ_{ss} are the coefficients of friction in the initial and steady states, respectively, and L_0 and L_w are the characteristic slip lengths for the constant and weakening regimes, respectively.

Similarly, the equation for height change $\Delta h(\delta)$ is given by:

$$\Delta h(\delta) = \Delta h_{ss} \left[1 - \exp\left(-\frac{\delta}{L_h}\right)\right], \quad (2)$$

where Δh_{ss} refers to the steady-state value of the height change, and L_h scales the characteristic length for the height decay.

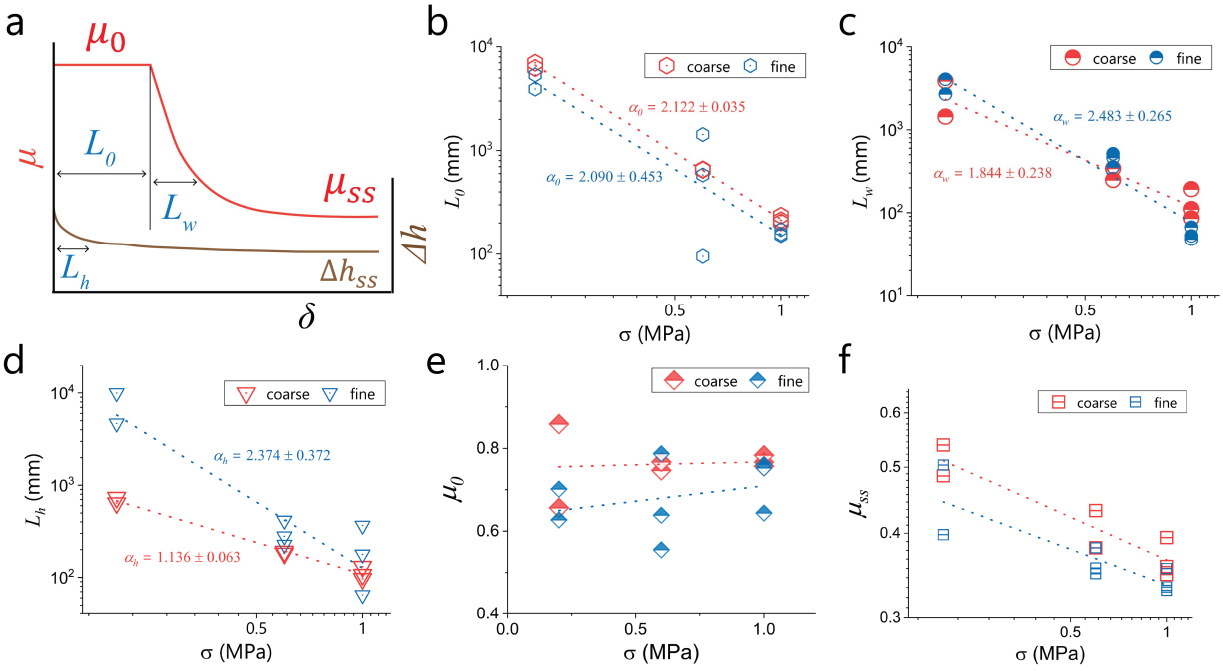

Figure 3. Effects of normal stress on characteristic slip lengths and frictional parameters. (a) Fitting of a frictional curve. The characteristic slip lengths for (b) the constant regime, (c)

weakening regime, and (d) height change against normal stress. (e) Constant friction coefficient and (f) Steady-state friction coefficient against normal stress.

The parameters in Equations (1) and (2) were estimated using nonlinear least-squares fitting (Table S1). The characteristic lengths L_0, L_w, and L_h were plotted against normal stress σ in Figures 3b, 3c, and 3d, respectively. They are all anticorrelated to σ. We obtained $L_0 \sim \sigma^{-\alpha_0}$, $L_w = \sigma^{-\alpha_w}$ and $L_h \sim \sigma^{-\alpha_h}$, where α_0, α_w, and α_h are constants. $\alpha_0 \approx 2$ and $\alpha_w \approx 2$ were approximately obtained from the fitting, regardless of the initial grain sizes. In contrast, α_h exhibited large variability based on the grain size.

In addition, μ_0 is independent of σ, as shown in Figure 3e. This agrees with Byerlee's or Coulomb-Amonton's law of friction. In contrast, μ_{ss} decreased with increasing σ, as seen in Figure 3f, suggesting that the two regimes are governed by different physical processes. μ_{ss} was generally lower in the fine-grained medium than in the coarse-grained medium. Note that some strengthening occurred at large slip displacements only under low-normal-stress conditions (e.g., run f02-2 in Figure S2). The experiments were conducted under room-dry conditions. Because NaCl is sensitive to moisture, moisture may assist in cohesion among grains, especially during significant grain size reduction. Additionally, cementation in the resultant shear zone blocks (see Figures 1b and 1c) may work similarly, which provides interesting topics for future studies.

4.2 Theoretical modeling

One outstanding characteristic of our experiments was that during grain comminution, many fine particles were produced in situ, filling the voids. The comminution rate was high when the normal stress was large. The initial large friction was due to large angular grains, and

steady-state friction was dominated by the friction of rounded fine particles, as spherical grains tend to have significantly low friction (e.g., Mair et al., 2002; Salerno et al., 2018). To understand the observed behavior and reproduce its characteristic features, we developed a theoretical model.

First, we considered the slip-displacement-dependent evolution of friction as follows:

$$\mu(\delta) = \frac{\sigma_{eff}(\delta)}{\sigma}\mu_0 + \left(1 - \frac{\sigma_{eff}(\delta)}{\sigma}\right)\mu_{ss}\,, \tag{3}$$

where μ_0 is the friction coefficient for the constant regime and is dominated by sliding friction of angular-shaped large grains, and μ_{ss} is the steady-state friction coefficient due to the rolling friction of rounded fine particles. $\sigma_{eff}\ (\delta)$ denotes the effective normal stress supported by large grains, which is considered equal to the applied normal stress σ in the early stage and decreases to zero with the progressive production of fine particles.

Subsequently, we introduce a wear process to consider the fine particles produced. To describe the wear process, we applied Archard's adhesion wear theory in tribology (Archard, 1953). In Archard's theory, wear volume Q is proportional to applied normal force F_N and

$$Q(\delta) \;=\; C\frac{F_N}{\sigma_Y}\,\delta, \tag{4}$$

sliding distance δ as:

where C is a dimensionless constant and σ_Y is the yield strength of the frictional material. Archard assumed that the real contact area was formed by plastic deformation of the asperities. The yield strength σ_Y of halite is ~10-30 MPa at room temperature (Picard et al., 2018), and its plastic deformation is significant in our experiments. Since F_N can be expressed by $F_N = A_0\,\sigma$,

where A_0 and σ are the nominal area of the ring-shaped shear zone and normal stress, respectively, Equation (4) can be re-written as the following formula:

$$Q(\delta) = CA_0 \frac{\sigma}{\sigma_Y} \delta, \quad (5)$$

For a granular medium, we assumed that the slip was evenly accommodated in multiple (N) layers within the shear zone. Thus, the real contact area becomes *N* times that of a single layer, and the slip in each layer is given by δ/N. In addition, we consider the effective normal stress for large grains and replace σ with σ_{eff}. Thus, Equation (5) can be expressed as:

$$Q(\delta) = C\, NA_0 \frac{\sigma_{eff}}{\sigma_Y} \frac{\delta}{N} = CA_0 \frac{\sigma_{eff}}{\sigma_Y} \delta. \quad (6)$$

Equation (6) is a smooth extension of Archard's equation for granular systems. Furthermore, we modified Equation (6) to fit our experimental data as follows:

$$Q(\delta) = CA_0 \left(\frac{\sigma_{eff}}{\sigma_Y}\right)^{\alpha} \delta. \quad (7)$$

Note Equation (7) recovers the original Archard's theory when $\alpha = 1$.

Next, we inferred that the comminuted fine particles accumulated in the voids between large grains during shearing (see Figure 4). Assume that the large grains were closely compacted as a porous medium (Figure 4a) with a constant packing fraction ϕ, within a shear zone of a given thickness, we have:

$$V_{void} = \frac{1-\phi}{\phi} V_{grain}, \quad (8)$$

and

$$V_{total} = \frac{1}{\phi} V_{grain}, \quad (9)$$

where V_{grain}, V_{void}, and $V_{total} = V_{grain} + V_{void}$ denote the grain, void, and bulk volumes, respectively, within a predefined shear zone.

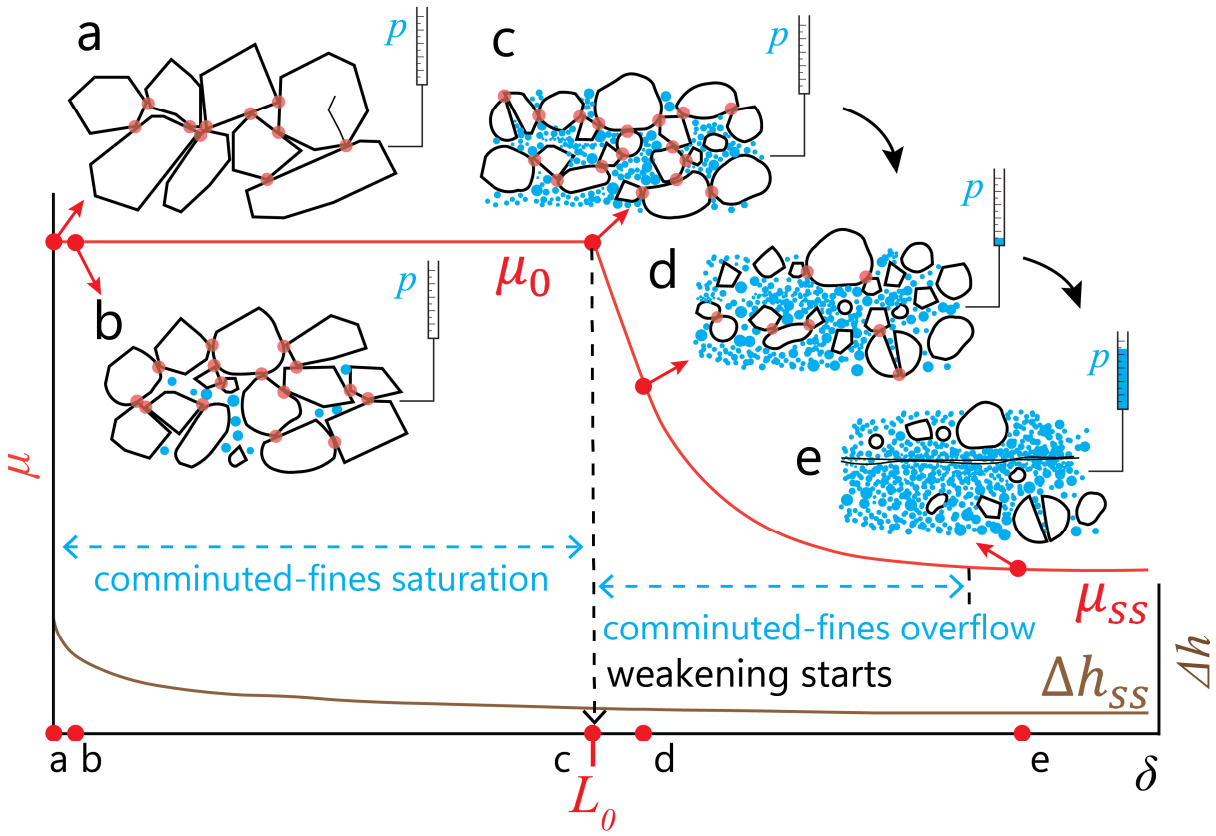

Figure 4. Weakening mechanisms. (a) Angular grains are compacted initially (red circles denote contacts between large grains) with zero pseudo fluid pressure ($p = \sigma - \sigma_{eff}$). (b) Intensive comminution starts once shear is imposed. (c) During shearing, angular large grains generate fine particles, which fill the voids between large grains at L_0. (d) Fine particles are continuously generated by grain comminution, overflow the shear zone, and decrease the effective normal stress between large grains. (e) Large grains are completely separated, and an extremely localized fine particle layer is formed.

The comminution of large grains was immediately initiated as shearing started (Figure 4b), and fine particles continued to accumulate in the voids within the shear zone until the comminuted fine particles saturated the entire shear zone (Figure 4c) at $\delta = L_0$. The saturation condition can be described by the balance between the void and wear volumes and by approximating the volume fraction of the fine grains by the same value ϕ:

$$\frac{1}{\phi} Q(L_0) = \frac{1-\phi}{\phi} (V_{grain,0} - Q(L_0)). \quad (10)$$

where $V_{grain,0}$ is the initial volume of large grains. Using Equations (9) and (10), $Q(L_0)$ can be written as

$$Q(L_0) = \frac{\phi(1-\phi)}{2-\phi} A_0 h_0 , \quad (11)$$

where h_0 denotes the initial height of the sample. By substituting Equation (7) into Equation (11) and $\sigma_{eff} = \sigma$ in this constant regime, L_0 is obtained as:

$$L_0 = \frac{h_0}{C} \frac{\phi(1-\phi)}{2-\phi} \left(\frac{\sigma}{\sigma_Y}\right)^{-\alpha} . \quad (12)$$

This result is consistent with our experimental results: $L_0 \sim \sigma^{-2}$ for $\alpha = 2$. The effect of initial grain size seems to be small, as shown in Figure 3b. The two media may have different characteristic shear-zone thicknesses, which may be defined by the shear-box dimensions, initial grain size, and normal stress. This may explain why the y-intercept yields a difference of approximately 40% (Figure 3b). Therefore, the characteristic thickness of the shear zone was postulated, and the motion of the fine particles was confined to this region. To simplify our analysis, we neglected dynamic effects, such as the loss of fine particles from the shear zone.

In addition, assuming that the sample compaction during shear can be attributed to height decay in the shear zone,

$$V_{total}(\delta) = A_0 \Delta h(\delta) = \frac{1}{\phi}\left(V_{grain,0} - Q(\delta)\right). \quad (13)$$

$\Delta h(\delta)$ is expressed as:

$$\Delta h(\delta) = -\frac{C}{\phi}\left(\frac{\sigma}{\sigma_Y}\right)^{\alpha} \delta\,. \quad (14)$$

We analyzed the dependence of $\Delta h(\delta)$ on normal stress σ and particle size d by estimating the initial height decay slope $\frac{d\Delta h}{d\delta}|_{\delta=0} = -\Delta h_{ss}/L_h$ (Figure S3 in the Supporting Information). $-\Delta h_{ss}/L_h$ appear to be proportional to σ^2 and $d^{0.3}$, which also realizes $\alpha = 2$ in Equation (14).

After saturation of fine particles in the shear zone, weakening started at $\delta = L_0$. We assumed that the comminution mechanism operated continuously and that the effective normal stress σ_{eff} decreased linearly with the wear volume, as follows:

$$\frac{dQ(\delta)}{d\delta} = \alpha - \beta Q(\delta)\,,\ \ \delta > L_0 \quad (15)$$

where α and β are constants. At the weakening point where saturation occurs, $Q = Q(L_0)$ and $\sigma_{eff} = \sigma$ are satisfied. Assume that the wear volume Q is m times $Q(L_0)$, namely $Q = mQ(L_0)$, when a steady state is achieved ($\frac{dQ}{d\delta} = 0$ and $\sigma_{eff} = 0$). Substituting Equation (15) into the differential form of Equation (7), we obtain:

$$\frac{dQ(\delta)}{d\delta} = \frac{CA_0}{m-1}\left(\frac{\sigma}{\sigma_Y}\right)^{\alpha}\left(m - \frac{Q(\delta)}{Q(L_0)}\right). \quad (16)$$

Integration leads to:

$$\ln\left(\frac{m-\frac{Q(\delta)}{Q(L_0)}}{m-1}\right) = -\frac{CA_0}{(m-1)Q(L_0)}\left(\frac{\sigma}{\sigma_Y}\right)^{\alpha}(\delta - L_0), \qquad \delta > L_0. \tag{17}$$

278 By substituting Equations (7) and (16) into Equation (17), we obtain:

$$\frac{\sigma_{eff}(\delta)}{\sigma} = \exp\left[-\frac{\delta - L_0}{\alpha(m-1)L_0}\right], \qquad \delta > L_0. \tag{18}$$

279 By substituting Equation (18) into Equation (3), we obtain:

$$\mu(\delta) = \mu_{ss} + (\mu_0 - \mu_{ss})\exp\left[-\frac{\delta - L_0}{\alpha(m-1)L_0}\right], \ \delta > L_0. \tag{19}$$

280 The characteristic length $L_w = \alpha(m-1)L_0$ is hitherto realized for the weakening regime. Using
281 Equation (12), we obtain:

$$L_w = \alpha(m-1)\frac{h_0}{C}\frac{\phi(1-\phi)}{2-\phi}\left(\frac{\sigma}{\sigma_Y}\right)^{-\alpha}. \tag{20}$$

282 We compared our theoretical calculations with the experimental results; the exponent $\alpha = 2$ is
283 again obtained, and $L_w \approx 0.5L_0$ (see Table S1) is recovered when $m = 5/4$.

284 The deviation of the exponent α ($= 2$ in our experiments) from the original Archard
285 theory ($= 1$) is not clear at this time. More detailed analyses are required in future studies.

286

287 **4.3 Shear localization mechanisms**

288 The above-mentioned model theoretically represents the normal stress-dependent
289 weakening behavior determined by grain comminution mechanisms. However, describing the
290 shear localization observed in the microstructures is insufficient. The microstructure revealed by
291 the micro-CT scan, shown in Figures 2c, 2d, and 2e, is similar to that observed in faults (e.g.,

Chester and Logan, 1986; Chester and Chester, 1998; Jefferies et al., 2006; Heilbronner and Keulen, 2006) and rock avalanche deposits (e.g., Davies et al., 1999; Crosta et al., 2007; McSaveney and Davies, 2007; Perinotto et al., 2015), in which layers of comminuted particles of various sizes and shapes are heterogeneously distributed in the shear zone.

One possible explanation is that while the sliding of large grains was initially distributed within the characteristic shear zone, a localized region developed near the shear box separation after the shear zone was saturated and compacted. The grains within this narrow domain undergo intensive comminution. This positive feedback enhances the localization and results in an extremely localized shear plane within the thin layer of fine grains, as shown in Figure 4e.

Another explanation is the grain segregation mechanism, which leads to characteristic textures such as inverse grading in rock avalanche deposits (e.g., Dunning, 2006; Crosta et al., 2007; Dufresne et al., 2016) and natural and experimental fault zones (Boullier et al., 2009; Ujiie and Tsutusmi, 2010). Siman-Tov and Brodsky (2018) reported gravity-independent segregation in experimental granular flows, where fine particles migrated symmetrically away from the source and affected the velocity structure. Based on the CT images, the dense upper layer and immature shear plane suggested upward migration (Figure 2c). The thick lower half of the shear zone suggests the role of the gravity-induced void-filling mechanism, possibly enhanced by stick-slip motions, where fine particles preferentially fall into the voids, as shown in Figures 2c, 2d, and 2e. Therefore, in situ comminuted fine particles can segregate from the source region and stabilize subsequent flow, which also leads to shear localization, as illustrated in Figure 4e. The migration of fine particles was likely dominated by the characteristic thickness, resulting in hard shear zone blocks within the granular medium (Figures 1b and 1c).

5 Conclusions

Friction experiments were performed on granular halite using a ring shear apparatus. We found that grain comminution was a key mechanism for determining the frictional behavior of a sheared granular system involving breakable grains. We proposed a simple mechanism for grain comminution: the generated fine particles gradually saturate the porous shear zone of the granular medium in a constant friction regime, and the overflow of fine particles leads to frictional weakening owing to the decrease in the effective normal stress between large grains and the interstitial flow of fine particles. In addition, we found that the intrinsic comminution and microstructure are similar to those of natural fault zones and rock avalanche deposits, suggesting their relevance and important implications for natural shear zones.

However, several problems remain unsolved: for instance, in situ observations of comminution behavior are lacking, and the mechanism responsible for determining the exponent $\alpha = 2$ and description of shear localization dynamics remain unknown. These results will be reported in future studies.

Acknowledgments

We acknowledge M. McSaveney, I. Doi, T. Hatano, N. Lapusta, and E. Brodsky for constructive discussions; T. Ma for elaborate coding guidance; and O. Tadai for micro-CT measurements. This study was funded by JSPS KAKENHI (No. JP21H05201, “Science of Slow to Fast Earthquakes”).

Open Research

The complete dataset and fitting code used in this study are available from Zenodo (https://doi.org/10.5281/zenodo.7898496). The figures were created using the open-source Python function matplotlib.pyplot, Origin 2023b, and Adobe Illustrator.

Author Contributions

Chengrui Chang (CC), Chao Huang (CH) and Yohei Hamada (YH) conducted the experiments. Hiroyuki Noda (HN) and Tetsuo Yamaguchi (TY) developed theoretical models. CC and TY drafted the manuscript. All authors participated in the discussion and review of the documents.

References

Archard, J. F. (1953). Contact and Rubbing of Flat Surfaces. Journal of Applied Physics, 24(8), 981–988. https://doi.org/10.1063/1.1721448

Borg, I., Friedman, M., Handin, J., & Higgs, D. V. (1960). Chapter 6: Experimental Deformation of St. Peter Sand: A Study of Cataclastic Flow. In *Geological Society of America Memoirs* (Vol. 79, pp. 133–192). Geological Society of America. https://doi.org/10.1130/MEM79-p133

Bos, B., & Spiers, C. J. (2002). Fluid-assisted Healing Processes in Gouge-bearing Faults: Insights from Experiments on a Rock Analogue System. *Pure and Applied Geophysics*, *159*(11–12), 2537–2566. https://doi.org/10.1007/s00024-002-8747-2

Boullier, A.-M., Yeh, E.-C., Boutareaud, S., Song, S.-R., & Tsai, C.-H. (2009). Microscale anatomy of the 1999 Chi-Chi earthquake fault zone. *Geochemistry, Geophysics, Geosystems*, *10*(3), Q03016. https://doi.org/10.1029/2008GC002252

Brace, W. F., & Byerlee, J. D. (1966). Stick-Slip as a Mechanism for Earthquakes. *Science*, *153*(3739), 990–992. https://doi.org/10.1126/science.153.3739.990

Buijze, L., Niemeijer, A. R., Han, R., Shimamoto, T., & Spiers, C. J. (2017). Friction properties and deformation mechanisms of halite(-mica) gouges from low to high sliding velocities. *Earth and Planetary Science Letters*, *458*, 107–119. https://doi.org/10.1016/j.epsl.2016.09.059

Chambon, G., Schmittbuhl, J., Corfdir, A., Orellana, N., Diraison, M., & Géraud, Y. (2006). The thickness of faults: From laboratory experiments to field scale observations. *Tectonophysics*, *426*(1–2), 77–94. https://doi.org/10.1016/j.tecto.2006.02.014

Chester, F. M., & Logan, J. M. (1986). Implications for mechanical properties of brittle faults from observations of the Punchbowl fault zone, California. *Pure and Applied Geophysics PAGEOPH*, *124*(1–2), 79–106. https://doi.org/10.1007/BF00875720

371 Chester, F. M, & Chester, J. S. (1998). Ultracataclasite structure and friction processes of the
372 Punchbowl fault, San Andreas system, California. *Tectonophysics*, *295*(1–2), 199–
373 221. https://doi.org/10.1016/S0040-1951(98)00121-8
374 Crosta, G. B., Frattini, P., & Fusi, N. (2007). Fragmentation in the Val Pola rock avalanche,
375 Italian Alps. *Journal of Geophysical Research: Earth Surface*, *112*(F1), F01006.
376 https://doi.org/10.1029/2005JF000455
377 Davies, T. R., & McSaveney, M. J. (2002). Dynamic simulation of the motion of fragmenting
378 rock avalanches. *Canadian Geotechnical Journal*, *39*(4), 789–798.
379 https://doi.org/10.1139/t02-035
380 Davies, T. R., & McSaveney, M. J. (2009). The role of rock fragmentation in the motion of
381 large landslides. *Engineering Geology*, *109*(1–2), 67–79.
382 https://doi.org/10.1016/j.enggeo.2008.11.004
383 Davies, T. R., McSaveney, M. J., & Hodgson, K. A. (1999). A fragmentation-spreading
384 model for long-runout rock avalanches. *Canadian Geotechnical Journal*, *36*(6), 1096–
385 1110. https://doi.org/10.1139/t99-067
386 Davies, T. R. H. (1982). Spreading of rock avalanche debris by mechanical fluidization. *Rock*
387 *Mechanics*, *15*(1), 9–24. https://doi.org/10.1007/BF01239474
388 Dieterich, J. H. (1972). Time-dependent friction in rocks. *Journal of Geophysical Research*,
389 *77*(20), 3690–3697. https://doi.org/10.1029/JB077i020p03690
390 Dieterich, J. H. (1978). Time-Dependent Friction and the Mechanics of Stick-Slip. In J. D.
391 Byerlee & M. Wyss (Eds.), *Rock Friction and Earthquake Prediction* (pp. 790–806).
392 Basel: Birkhäuser. https://doi.org/10.1007/978-3-0348-7182-2_15
393 Dieterich, J. H. (1981). Potential for geophysical experiments in large scale tests.
394 *Geophysical Research Letters*, *8*(7), 653–656.
395 https://doi.org/10.1029/GL008i007p00653

Dufresne, A., Bösmeier, A., & Prager, C. (2016). Sedimentology of rock avalanche deposits – Case study and review. *Earth-Science Reviews*, *163*, 234–259. https://doi.org/10.1016/j.earscirev.2016.10.002

Dunning, S. A. (2006). The grain size distribution of rock-avalanche deposits in valley-confined settings. *Italian Journal of Engineering Geology and Environment*, (2006), 117–121. https://doi.org/10.4408/IJEGE.2006-01.S-15

Engelder, J. T. (1974). Cataclasis and the Generation of Fault Gouge. *Geological Society of America Bulletin*, *85*(10), 1515. https://doi.org/10.1130/0016-7606(1974)85<1515:CATGOF>2.0.CO;2

Faulkner, D. R., Jackson, C. A. L., Lunn, R. J., Schlische, R. W., Shipton, Z. K., Wibberley, C. A. J., & Withjack, M. O. (2010). A review of recent developments concerning the structure, mechanics and fluid flow properties of fault zones. *Journal of Structural Geology*, *32*(11), 1557–1575. https://doi.org/10.1016/j.jsg.2010.06.009

Fossen, H. (2010). *Structural Geology*. Cambridge: Cambridge University Press. https://doi.org/10.1017/CBO9780511777806

Griggs, D., & Handin, J. (1960). Chapter 13: Observations on Fracture and a Hypothesis of Earthquakes. In *Geological Society of America Memoirs* (Vol. 79, pp. 347–364). Geological Society of America. https://doi.org/10.1130/MEM79-p347

Heilbronner, R., & Keulen, N. (2006). Grain size and grain shape analysis of fault rocks. *Tectonophysics*, *427*(1–4), 199–216. https://doi.org/10.1016/j.tecto.2006.05.020

Heim, A. (1932). Bergsturz und Menschenleben. Zürich: Fretz und Wasmuth, 218.

Hiraga, H., & Shimamoto, T. (1987). Textures of sheared halite and their implications for the seismogenic slip of deep faults. *Tectonophysics*, *144*(1), 69–86. https://doi.org/10.1016/0040-1951(87)90009-6

Hsü, K. J. (1975). Catastrophic Debris Streams (Sturzstroms) Generated by Rockfalls. *Geological Society of America Bulletin*, *86*(1), 129. https://doi.org/10.1130/0016-7606(1975)86<129:CDSSGB>2.0.CO;2

Hu, W., Xu, Q., McSaveney, M., Scaringi, G., Huang, R., Wang, G., et al. (2022). Fluid-Like Behavior of Crushed Rock Flows. *Journal of Geophysical Research: Earth Surface*, *127*(10). https://doi.org/10.1029/2021JF006523

Jefferies, S. P., Holdsworth, R. E., Shimamoto, T., Takagi, H., Lloyd, G. E., & Spiers, C. J. (2006). Origin and mechanical significance of foliated cataclastic rocks in the cores of crustal-scale faults: Examples from the Median Tectonic Line, Japan. *Journal of Geophysical Research: Solid Earth*, *111*(B12). https://doi.org/10.1029/2005JB004205

Kim, J.-W., Ree, J.-H., Han, R., & Shimamoto, T. (2010). Experimental evidence for the simultaneous formation of pseudotachylyte and mylonite in the brittle regime. *Geology*, *38*(12), 1143–1146. https://doi.org/10.1130/G31593.1

Kimura, G., Kitamura, Y., Hashimoto, Y., Yamaguchi, A., Shibata, T., Ujiie, K., & Okamoto, S. (2007). Transition of accretionary wedge structures around the up-dip limit of the seismogenic subduction zone. *Earth and Planetary Science Letters*, *255*(3–4), 471–484. https://doi.org/10.1016/j.epsl.2007.01.005

Kitajima, H., & Saffer, D. M. (2014). Consolidation state of incoming sediments to the Nankai Trough subduction zone: Implications for sediment deformation and properties. *Geochemistry, Geophysics, Geosystems*, *15*(7), 2821–2839. https://doi.org/10.1002/2014GC005360

Legros, F. (2002). The mobility of long-runout landslides. *Engineering Geology*, *63*(3–4), 301–331. https://doi.org/10.1016/S0013-7952(01)00090-4

443 Mair, K., Frye, K. M., & Marone, C. (2002). Influence of grain characteristics on the friction
444 of granular shear zones. *Journal of Geophysical Research: Solid Earth*, *107*(B10),
445 ECV 4-1-ECV 4-9. https://doi.org/10.1029/2001JB000516
446 Mclaskey, G. C., & Yamashita, F. (2017). Slow and fast ruptures on a laboratory fault
447 controlled by loading characteristics. *Journal of Geophysical Research: Solid Earth*,
448 *122*(5), 3719–3738. https://doi.org/10.1002/2016JB013681
449 McSaveney, M., & Davies, T. (2007). Rockslides and their motion. In *Progress in Landslide*
450 *Science* (pp. 113–133). Berlin, Heidelberg: Springer. https://doi.org/10.1007/978-3-
451 540-70965-7_8
452 Noda, H., & Shimamoto, T. (2010). A rate- and state-dependent ductile flow law of
453 polycrystalline halite under large shear strain and implications for transition to brittle
454 deformation. *Geophysical Research Letters*, *37*(9), L09310.
455 https://doi.org/10.1029/2010GL042512
456 Noda, H., & Shimamoto, T. (2012). Transient behavior and stability analyses of halite shear
457 zones with an empirical rate-and-state friction to flow law. *Journal of Structural*
458 *Geology*, *38*, 234–242. https://doi.org/10.1016/j.jsg.2011.08.012
459 Perinotto, H., Schneider, J., Bachèlery, P., Le Bourdonnec, F., Famin, V., & Michon, L.
460 (2015). The extreme mobility of debris avalanches: A new model of transport
461 mechanism. *Journal of Geophysical Research: Solid Earth*, *120*(12), 8110–8119.
462 https://doi.org/10.1002/2015JB011994
463 Picard, D., Dimanov, A., & Raphanel, J. L. (2018). Plastic behavior of halite single-crystals
464 at different temperatures and strain rates: New insights from in-situ experiments and
465 full field measures. *Materials Science and Engineering: A*, *732*, 284–297.
466 https://doi.org/10.1016/j.msea.2018.07.009

Polet, J., & Kanamori, H. (2000). Shallow subduction zone earthquakes and their tsunamigenic potential. *Geophysical Journal International*, *142*(3), 684–702. https://doi.org/10.1046/j.1365-246x.2000.00205.x

Robertson, E. C. (1982). Continuous formation of gouge and breccia during fault displacement. In: The 23rd U.S Symposium on Rock Mechanics (USRMS)

Salerno, K. M., Bolintineanu, D. S., Grest, G. S., Lechman, J. B., Plimpton, S. J., Srivastava, I., & Silbert, L. E. (2018). Effect of shape and friction on the packing and flow of granular materials. *Physical Review E*, *98*(5), 050901. https://doi.org/10.1103/PhysRevE.98.050901

Sassa, K., & Lee, J.-H. (1993). Measurement of the apparent friction angle during motion by the high-speed ring shear apparatus. *Landslides*, *30*(1), 1-10_1. https://doi.org/10.3313/jls1964.30.1

Sassa, K., Fukuoka, H., Scarascia-Mugnozza, G., & Evans, S. (1996). Earthquake-Induced-Landslides: Distribution, Motion and Mechanisms. *Soils and Foundations*, *36*(Special), 53–64. https://doi.org/10.3208/sandf.36.Special_53

Sassa, K., Fukuoka, H., Wang, G., & Ishikawa, N. (2004). Undrained dynamic-loading ring-shear apparatus and its application to landslide dynamics. *Landslides*, *1*(1), 7–19. https://doi.org/10.1007/s10346-003-0004-y

Scholz, C. H. (1987). Wear and gouge formation in brittle faulting. *Geology*, *15*(6), 493. https://doi.org/10.1130/0091-7613(1987)15<493:WAGFIB>2.0.CO;2

Shimamoto, T. (1986). Transition between frictional slip and ductile flow for halite shear zones at room temperature. *Science*, *231*(4739), 711–714. https://doi.org/10.1126/science.231.4739.711

Shimamoto, T., Handin, J., & Logan, J. M. (1980). Specimen-apparatus interaction during stick-slip in a triaxial compression machine: A decoupled two-degree-of-freedom

492 model. *Tectonophysics*, *67*(3–4), 175–205. https://doi.org/10.1016/0040-
493 1951(80)90234-6
494 Sibson, R. H. (2003). Thickness of the Seismic Slip Zone. *Bulletin of the Seismological*
495 *Society of America*, *93*(3), 1169–1178. https://doi.org/10.1785/0120020061
496 Siman-Tov, S., & Brodsky, E. E. (2018). Gravity-Independent Grain Size Segregation in
497 Experimental Granular Shear Flows as a Mechanism of Layer Formation.
498 *Geophysical Research Letters*, *45*(16), 8136–8144.
499 https://doi.org/10.1029/2018GL078486
500 Tsutsumi, A., & Shimamoto, T. (1997). High-velocity frictional properties of gabbro.
501 *Geophysical Research Letters*, *24*(6), 699–702. https://doi.org/10.1029/97GL00503
502 Ujiie, K., & Tsutsumi, A. (2010). High-velocity frictional properties of clay-rich fault gouge
503 in a megasplay fault zone, Nankai subduction zone. *Geophysical Research Letters*,
504 *37*(24). https://doi.org/10.1029/2010GL046002
505 von Kármán. (1911). Festigkeitsversuche unter allseitigem Drunk. *Zeitschrift de Vereines*
506 *deutscher Ingenieure*, *55*, 1749.
507 Weeks, J. D., & Tullis, T. E. (1985). Frictional sliding of dolomite: A variation in constitutive
508 behavior. *Journal of Geophysical Research: Solid Earth*, *90*(B9), 7821–7826.
509 https://doi.org/10.1029/JB090iB09p07821
510 Yamashita, F., Fukuyama, E., Mizoguchi, K., Takizawa, S., Xu, S., & Kawakata, H. (2015).
511 Scale dependence of rock friction at high work rate. *Nature*, *528*(7581), 254–257.
512 https://doi.org/10.1038/nature16138
513

514 **References from the Supporting Information**

515 Kawakata, H., Cho, A., Kiyama, T., Yanagidani, T., Kusunose, K., & Shimada, M. (1999).
516 Three-dimensional observations of faulting process in Westerly granite under uniaxial

517 and triaxial conditions by X-ray CT scan. *Tectonophysics*, *313*(3), 293–305.
518 https://doi.org/10.1016/S0040-1951(99)00205-X
519 Raynaud, S., Fabre, D., Mazerolle, F., Geraud, Y., & Latière, H. J. (1989). Analysis of the
520 internal structure of rocks and characterization of mechanical deformation by a non-
521 destructive method: X-ray tomodensitometry. *Tectonophysics*, *159*(1–2), 149–159.
522 https://doi.org/10.1016/0040-1951(89)90176-5